An Automatic Framework for Segmentation of Brain Tumours at Follow-up Scans after Radiation Therapy*

Elham Karami, Ali Jalalifar, Mark Ruschin, Hany Soliman, Arjun Sahgal, Greg J. Stanisz, and Ali Sadeghi-Naini, *Senior Member, IEEE*

Abstract— **Brain metastasis is the most common intracranial malignancy with a poor overall survival (OS) after treatment. The standard stereotactic radiation therapy (SRT) planning procedure for brain metastasis requires delineating the tumour volume on magnetic resonance (MR) images. MR images are also acquired at multiple follow-up scans after SRT to monitor the treatment outcome through measuring changes in the physical dimensions of the tumour. Such measurements require manual segmentation of the tumour volume on multiple slices of several follow-up images which is tedious and impedes the SRT evaluation work flow considerably. In this study, an automatic framework was proposed to segment the tumour volume on longitudinal MR images acquired at standard follow-up scans after SRT. The multi-step segmentation framework was based on region growing and morphological snakes models that applied the standard SRT planning tumour contour as a basis to approximate the tumour shape and location at each follow-up scan for an accurate automatic segmentation of tumour volume. The framework was evaluated using the MR imaging data acquired from five patients prior to and at three follow-up scans after SRT. The preliminary results indicated that the Dice similarity coefficient between the ground truth tumour masks and their automatically segmented counterparts ranged between 0.84 and 0.90, while the average Dice coefficient for all the follow-up scans was 0.88. The results obtained implied a good potential of the proposed framework for being incorporated into the SRT treatment planning and evaluation systems as well as outcome prediction models.**

*This research was supported by Natural Sciences and Engineering Research Council (NSERC) of Canada, Canadian Institutes for Health Research (CIHR), and Terry Fox Foundation.

E. Karami is with the Department of Medical Biophysics, University of Toronto, Toronto, ON, Canada; also with the Physical Sciences Platform, Sunnybrook Research Institute, Sunnybrook Health Sciences Centre, Toronto, ON, Canada (e-mail: elham.karami@sri.utoronto.ca).

A. Jalalifar is with the Department of Electrical Engineering and Computer Science, Lassonde School of Engineering, York University, Toronto, ON, Canada (e-mail: alijfar@yorku.ca).

M. Ruschin, H. Soliman, and A. Sahgal are with the Department of Radiation Oncology, Odette Cancer Centre, Sunnybrook Health Sciences Centre, Toronto, ON, Canada; also with the Department of Radiation Oncology, University of Toronto, Toronto, ON, Canada (e-mail: mark.ruschin@sunnybrook.ca; hany.soliman@sunnybrook.ca; arjun.sahgal@sunnybrook.ca).

G. Stanisz is with the Department of Medical Biophysics, University of Toronto, Toronto, ON, Canada; also with the Physical Sciences Platform, Sunnybrook Research Institute, Sunnybrook Health Sciences Centre, Toronto, ON, Canada (e-mail: stanisz@sri.utoronto.ca)

A. Sadeghi-Naini is with the Department of Electrical Engineering and Computer Science, York University, Toronto, ON, Canada; also with the Department of Radiation Oncology and Physical Sciences Platform, Odette Cancer Centre and Sunnybrook Research Institute, Sunnybrook Health Sciences Centre, Toronto, ON, Canada; also with the Department of Medical Biophysics, University of Toronto, Toronto, ON, Canada (e-mail: asn@yorku.ca, phone: 416-736-2100 x20590).

I. Introduction

Brain metastasis is the most common intracranial malignancy in both men and woman [1] . Depending on the size, number of tumours and other disease characteristics, the brain metastasis patients are treated with whole-brain radiation therapy (WBRT), stereotactic radiation therapy (SRT), surgical resection, and/or systemic therapy [2]. Recent studies have demonstrated that SRT is associated with less brain damage than WBRT, and as a result it has now become the standard treatment method for patients having less than 10 brain lesions [3]. However, up to 20% of metastatic brain tumours fail to respond to standard radiation therapy [4].

Gadolinium contrast-enhanced magnetic resonance (MR) images are conventionally used by radiation oncologists to delineate the tumour volume in radiation treatment planning for brain metastasis. MR images are also acquired at multiple sessions after the treatment as part of the standard follow-up assessment. The local response of the tumour to SRT is determined using the follow-up imaging data mainly based on the changes in physical measurements of the tumour. In this context, a tumour is considered to have a local failure (LF) outcome if a consistent progression or recurrence is detected at the treated site. Similarly, a local control (LC) outcome for a tumour is determined if the lesion size is stable, decreased, or increased initially followed by a consistent decrease (pseudo-progression). As such, to monitor and evaluate the LC/LF outcome of the treatment, it is required to segment the entire tumour volume on the follow-up images. Since the follow-up imaging intervals for the brain metastasis patients are relatively short, clinicians are often required to segment each tumour on several longitudinal images that is tedious and time consuming. An automatic segmentation framework can considerably streamline the radiation therapy evaluation workflow.

In addition to routine outcome assessments, an automatic segmentation framework is highly in demand for developing radiomics-based predictive models of therapy response and outcome [5]–[9]. Radiomics refers to high-throughput mining of medical images that applies data-driven computational methods to extract and explore quantitative biomarkers from medical images for specific diagnostic and/or prognostic applications [5], [10]–[15]. In the context of cancer therapeutics, radiomics models require tumour segmentation on different images (e.g. pre- and post-contrast T1-weighted, T2-weighted and T2-FLAIR images of brain) acquired from a large cohort of patients [8]. The segmented tumour masks are subsequently used for quantitative feature extraction and analysis. An automatic framework for tumour segmentation can considerably facilitate development and

978-1-5386-1311-5/19/$31.00 ©2019 IEEE

incremental adjustment of radiomics models for brain tumours.

Automatic segmentation of brain tumours in longitudinal follow-up images after SRT is, however, challenging. The shape, size, and intensity of the tumour in MR images may alter significantly in response to radiation therapy or as a result of tumour progression or recurrence [16]. Therefore, whereas an approximate location of tumour is available from the previous scans, the tumour volume segmentation should be updated precisely at each follow-up.

In this study, an automatic framework was proposed for segmentation of metastatic brain tumours on follow-up gadolinium contrast-enhanced T1-weighted (T1w) images acquired after SRT. The tumour outline, delineated by expert oncologists as part of the standard treatment planning, was initially registered to the follow-up images. The registered tumour outline that approximated the location of the tumour at the follow-up scan was then used as the initial contour for a deformable model-based segmentation technique. Subsequently, a precise contour of the tumour on each axial slice of the image was generated. The framework was evaluated using data acquired from five patients prior to and at three follow-ups after the treatment. The quantitative results indicated that the framework could segment the tumours with an average Dice similarity coefficient of 0.88, 0.88 and 0.87 compared to the manual contours, for the first, second and third follow- up scans, respectively.

II. Methods

A. Dataset

This study was conducted in accordance with institutional research ethics board approval from Sunnybrook Health Sciences Centre (SHSC), Toronto, Canada. The imaging data were collected from five patients diagnosed with brain metastasis, and treated with hypo-fractionated SRT. The dataset included the T1w images acquired immediately before the treatment (baseline) and at three follow-up scans after the treatment. The baseline and follow-up images were acquired as part of the institutional standard of care for patients with brain metastasis.

Each follow-up image was acquired within a few months from the previous scan (mean: 2.2 months; range: 1 to 3.8 months). The in-plane image resolution and the slice thickness were 0.5 and 1.5 mm, respectively. The dataset also included the baseline tumour contours for each patient, delineated by expert oncologists. The manual tumour contours for the follow-up images were delineated under the supervision of an expert oncologist and used as the ground truth to evaluate the performance of the proposed segmentation framework.

B. Segmentation Framework

The proposed segmentation framework applied the *a priori* information available from the baseline tumour contour to find an approximate location and shape of the tumour in the longitudinal follow-up images. For this purpose, the baseline image was registered to all follow-up images using an affine registration method with mutual information (MI) as the similarity metric [17]. The registration transformation matrix was subsequently used to warp the baseline tumour contour on each follow-up image. The registration and warping algorithms were implemented in the ITK software toolkit.

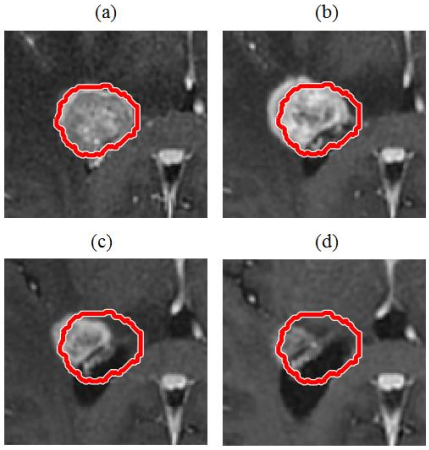

Figure 1. An SRT planning tumour contour overlaied on the T1w images at the basleine (a), and the first (b), second (c) and third (d) follow-ups.

Fig. 1(a) demonstrates an example of a baseline image with the tumour contour outlined by an oncologist. Figs. 1(b), (c), and (d) show the baseline tumour contour registered on the three follow-up images.

The registered tumour outline was used to find a set of seeds for a region-growing algorithm to segment the tumour crudely [18]. Next, the projections of the tumour in x, y, and z directions were used to crop an ROI containing the tumour. Finally, the registered tumour outline was used as an initial contour for a deformable model-based segmentation to segment the tumour region accurately on each axial slice. Specifically, the algorithm started from the middle slice of the tumour and used the baseline tumour outline as the initial contour to segment the tumour area precisely. Subsequently, moving from the middle slice in the inferior and superior directions, in each slice the algorithm applied the segmentation result of the previous slice as the initial contour for the deformable model-based segmentation of the tumour.

A morphological "snakes" model was used for the deformable model-based segmentation in each slice [19], [20]. The morphological snakes model is similar to the active contours model which fits a deformable contour to an object iteratively [21], [22]. The traditional approaches for active contours require solving partial differential equations (PDEs) over floating point arrays at each iteration. Such approaches are slow and have demonstrated to be unstable in some applications [23]. To address these issues, the morphological snakes use morphological operators such as dilation and erosion instead of PDEs to deform a contour iteratively. As such, the morphological snakes are potentially faster and numerically more stable compared to their traditional counterparts. The dilation D_h , and erosion E_h of function u with radius h are defined as

$$D_h u(x) = \sup_{y \in hb(0,1)} u(x+y), \quad (1)$$

and

$$E_h u(x) = \inf_{y \in hb(0,1)} u(x+y), \quad (2)$$

where *sup* and *inf* are the supremum and infimum of the function u. In both definitions, $b(0,1)$ is a ball structuring

element of radius 1 centred at 0. The set b is scaled by the radius h, *i.e.* $hb = \{hx: x \in b\}$. Using mathematical morphology, every morphological operator T can be represented using a $sup - inf$ form [19]:

$$(T_h u)(x) = \underset{b\in B}{sup}\ \underset{y\in x+hb}{inf}\ u(y), \quad (3)$$

or a dual $inf - sup$ representation [19]:

$$(T_h u)(x) = \underset{b\in B}{inf}\ \underset{y\in x+hb}{sup}\ u(y). \quad (4)$$

In both representations, B is a set of structuring elements that uniquely defines the operator, and h is the size of the operator.

1) The 2D curvature morphological operator

A number of morphological operators can be expressed as PDEs. Therefore, the deformable model PDEs can be approximated using appropriate morphological operators. In particular, it has been demonstrated that the curvature flow of the PDE $\frac{\partial u}{\partial t} = div(\frac{\nabla u}{|\nabla u|}).|\nabla u|$ can be approximated using the successive application of the morphological mean operator $F_{\sqrt{h}}$ [24], where

$$(F_h u)(x) = \frac{(SI_{2h}u)(x)+(IS_{2h}u)(x)}{2}. \quad (5)$$

In (5) SI_h and IS_h are the $sup - inf$ and $inf - sup$ morphological operators given by the base $B^2 = \{[-1,1]_\theta \subset \mathbb{R}^2: \theta \in [0,\pi)\}$ made of all segments of length 2 centered at the origin.

Since the operator F_h is not contrast-invariant, it is not a morphological operator. However, $F_{\sqrt{h}}$ can be approximated by the composition $SI_{\sqrt{h}} \circ IS_{\sqrt{h}}$ which is the curvature morphological operator [19].

2) Morphological active contours without edges (ACWE)

The well-known PDE of the ACWE is as follows:

$$\frac{\partial u}{\partial t} = |\nabla u|(\mu div(\frac{\nabla u}{|\nabla u|}) - \nu - \lambda_1(I - c_1)^2 - \lambda_2(I - c_2)^2)) \quad (6)$$

Given the hyper-surface status at iteration n, $u^n: \mathbb{Z}^d \to \{0,1\}$, the morphological ACWE is given by the following three steps:

$$u^{n+\frac{1}{3}}(x) = \begin{cases} (D_d u^n)(x) & if\ \nu > 0 \\ (E_d u^n)(x) & if\ \nu < 0 \\ (u^n)(x) & otherwise \end{cases}$$

$$u^{n+\frac{2}{3}}(x) = \begin{cases} 1 & if\ |\nabla u^{n+\frac{1}{3}}|(\lambda_1(I - c_1)^2 - \lambda_2(I - c_2)^2)(x) < 0 \\ 0 & if\ |\nabla u^{n+\frac{1}{3}}|(\lambda_1(I - c_1)^2 - \lambda_2(I - c_2)^2)(x) > 0 \\ u^{n+\frac{1}{3}} & otherwise \end{cases}$$

$$u^{n+1}(x) = ((SI_d \circ IS_d)^\mu u^{n+\frac{2}{3}})(x) \quad (7)$$

Equation (7) can be used to minimize the ACWE cost function in a fast, simple, stable and robust method. In this work, the parameters n, λ_1 , λ_2, μ, and ν were set to 100, 1, 1, 2, and 0, respectively.

III. Results

Automatic segmentation of the entire tumour volume on each follow-up image took about 30 seconds on average, using a computer with an Intel Core i5 processor and 8 GB of RAM. The segmentation results obtained for each follow-up scan are shown for the five tumours in Fig. 2. The red, blue, and purple masks represent the manually (ground truth) and automatically segmented regions, and their overlap area, respectively. Qualitatively, the results obtained from the segmentation framework agree well with the ground truth. The dataset included a very challenging case where the tumour was located close to the ventricles (patient 2). As observed in Fig. 2, the framework could successfully outline the shrinking tumour at all follow-up scans with results comparable with those obtained for the other tumours.

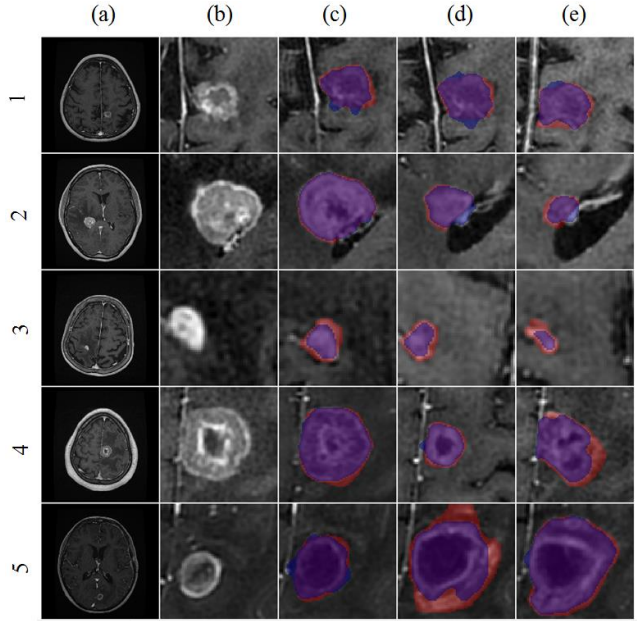

Figure 2. An axial cross-section image of each tumour (first to fifth rows) at the baseline (a, b) , as well as the first (c), second (d), and third (e) follow-up scan. The red , blue, and purple masks represent the manual, automatically segmented, and the overlap regions, respectively.

Table I presents the quantitative results of the automatic tumour segmentation in terms of Dice similarity coefficient for the 5 patients. The average Dice similarity coefficient between the manual and automatic tumour contours of the five patients ranged between 0.87 to 0.90 for the first follow-up, 0.85 to 0.90 for the second follow-up, and 0.84 to 0.89 for the third follow-up scans. The average Dice coefficient for all patients was 0.88, 0.88 and 0.87 for the first, second,

TABLE I. The Dice similarity coefficient for segmentation at different follow-up (FU) scans.

Patient number	Dice similarity coefficient		
	1st FU	*2nd FU*	*3rd FU*
1	0.87 ± 0.05	0.88 ± 0.07	0.89 ± 0.06
2	0.88 ± 0.06	0.85 ± 0.05	0.84 ± 0.06
3	0.90 ± 0.03	0.90 ± 0.03	0.88 ± 0.04
4	0.90 ± 0.06	0.89 ± 0.06	0.87 ± 0.07
5	0.87 ± 0.05	0.87 ± 0.05	0.88 ± 0.06
Mean ± SD	0.88 ± 0.05	0.88 ± 0.05	0.87 ± 0.06

and third follows-up scans respectively. Table II presents the average distance between the two contours throughout all 2D slices of each follow-up image. The average distance obtained for the first, second and third follow-up scans of all patients were 0.29, 0.28 and 0.28 mm, respectively.

IV. Discussion

In this study, a framework was proposed for automatic segmentation of the malignancies on T1w follow-up images acquired after the SRT as part of the standard of care for brain metastasis patients. The proposed framework was based on a 2D morphological snakes model that applied the SRT planning tumour contours as *a priori* information to approximate the tumour shape and location in the follow-up images. The framework was evaluated using the MR imaging data acquired from five patients at the baseline and three follow-up scans. The quantitative comparison between the ground truth masks and their automatically generated counterparts indicated an average Dice similarity coefficient and average distance of 0.88 and 0.28 mm, respectively, for all follow-up scans.

The presented technique can potentially be used for automatic LC/LF outcome determination, as well as treatment planning in case of progression or recurrence at the tumour site. Another application of the proposed framework is in radiomics-based outcome prediction modeling where the tumour mask is required for extracting the quantitative features. The results obtained in this proof-of-principle study encourage further evaluation of the proposed framework and comparison with other segmentation methods such as convolutional neural networks, on a larger cohort of patients.

TABLE II. The Average distance for segmentationat At different follow-up (FU) scans.

Patient number	Average distance (mm)		
	1st FU	*2nd FU*	*3rd FU*
1	0.30 ± 0.02	0.32 ± 0.04	0.33 ± 0.03
2	0.39 ± 0.08	0.30 ± 0.07	0.25 ± 0.06
3	0.11 ± 0.02	0.10 ± 0.02	0.17 ± 0.09
4	0.34 ± 0.06	0.21 ± 0.03	0.36 ± 0.07
5	0.32 ± 0.05	0.48 ± 0.10	0.29 ± 0.08
Mean ± SD	0.29 ± 0.11	0.28 ± 0.14	0.28 ± 0.07

References

[1] Q. T. Ostrom, C. H. Wright, and J. S. Barnholtz-Sloan, "Brain metastases: epidemiology," in *Handbook of Clinical Neurology*, vol. 149, 2018, pp. 3–23.

[2] M. Tsao, W. Xu, and A. Sahgal, "A meta-analysis evaluating stereotactic radiosurgery, whole-brain radiotherapy, or both for patients presenting with a limited number of brain metastases," *Cancer*, vol. 118, no. 9, pp. 2486–93, May 2012.

[3] M. Yamamoto, T. Serizawa, T. Shuto, A. Akabane, Y. Higuchi, *et al.* "Stereotactic radiosurgery for patients with multiple brain metastases (JLGK0901): a multi-institutional prospective observational study," *Lancet. Oncol.*, vol. 15, no. 4, pp. 387–95, Apr. 2014.

[4] G. Minniti, C. Scaringi, S. Paolini, G. Lanzetta, A. Romano, *et al.* "Single-Fraction Versus Multifraction (3 × 9 Gy) Stereotactic Radiosurgery for Large (>2 cm) Brain Metastases: A Comparative Analysis of Local Control and Risk of Radiation-Induced Brain Necrosis," *Int. J. Radiat. Oncol.*, vol. 95, no. 4, pp. 1142–1148, Jul. 2016.

[5] A. Sadeghi-Naini, O. Falou, H. Tadayyon, A. Al-Mahrouki, W. Tran, N. Papanicolau, M. C. Kolios, and G. J. Czarnota, "Conventional frequency ultrasonic biomarkers of cancer treatment response in vivo," *Transl. Oncol.*, vol. 6, no. 3, pp. 234–243, Jun. 2013.

[6] A. Sadeghi-Naini, O. Falou, J. M. Hudson, C. Bailey, P. N. Burns, M. J. Yaffe, G. J. Stanisz, M. C. Kolios, and G. J. Czarnota, "Imaging innovations for cancer therapy response monitoring," *Imaging Med.*, vol. 4, no. 3, pp. 311–327, Jun. 2012.

[7] H. J. W. L. Aerts, E. R. Velazquez, R. T. H. Leijenaar, C. Parmar, P. Grossmann, *et al.* "Decoding tumour phenotype by noninvasive imaging using a quantitative radiomics approach," *Nat. Commun.*, vol. 5, 2014.

[8] Q. Li, H. Bai, Y. Chen, Q. Sun, L. Liu, S. Zhou, G. Wang, C. Liang, and Z. C. Li, "A Fully-Automatic Multiparametric Radiomics Model: Towards Reproducible and Prognostic Imaging Signature for Prediction of Overall Survival in Glioblastoma Multiforme," *Sci. Rep.*, vol. 7, no. 1, pp. 1–9, 2017.

[9] A. Sadeghi-Naini, E. Vorauer, L. Chin, O. Falou, W. T. Tran, F. C. Wright, S. Gandhi, M. J. Yaffe, and G. J. Czarnota, "Early detection of chemotherapy-refractory patients by monitoring textural alterations in diffuse optical spectroscopic images," *Med. Phys.*, vol. 42, no. 11, pp. 6130–6146, Nov. 2015.

[10] R. J. Gillies, P. E. Kinahan, and H. Hricak, "Radiomics: Images Are More than Pictures, They Are Data," *Radiology*, vol. 278, no. 2, pp. 563–577, 2016.

[11] A. Sadeghi-Naini, L. Sannachi, H. Tadayyon, W. T. Tran, E. Slodkowska, M. Trudeau, S. Gandhi, K. Pritchard, M. C. Kolios, and G. J. Czarnota, "Chemotherapy-Response Monitoring of Breast Cancer Patients Using Quantitative Ultrasound-Based Intra-Tumour Heterogeneities," *Sci. Rep.*, vol. 7, p. 10352, 2017.

[12] W. T. Tran, M. J. Gangeh, L. Sannachi, L. Chin, E. Watkins, *et al.* "Predicting breast cancer response to neoadjuvant chemotherapy using pretreatment diffuse optical spectroscopic texture analysis," *Br. J. Cancer*, vol. 116, no. 10, pp. 1329–1339, 2017.

[13] M. J. Gangeh, H. Tadayyon, L. Sannachi, A. Sadeghi-Naini, W. T. Tran, and G. J. Czarnota, "Computer Aided Theragnosis Using Quantitative Ultrasound Spectroscopy and Maximum Mean Discrepancy in Locally Advanced Breast Cancer," *IEEE Trans. Med. Imaging*, vol. 35, no. 3, pp. 778–790, 2016.

[14] H. Tadayyon, L. Sannachi, M. J. Gangeh, C. Kim, S. Ghandi, *et al.* "A priori prediction of neoadjuvant chemotherapy response and survival in breast cancer patients using quantitative ultrasound," *Sci. Rep.*, vol. 7, p. 45733, 2017.

[15] A. Sadeghi-Naini, E. Sofroni, N. Papanicolau, O. Falou, L. Sugar, G. Morton, M. J. Yaffe, R. Nam, A. Sadeghian, M. C. Kolios, H. T. Chung, and G. J. Czarnota, "Quantitative ultrasound spectroscopic imaging for characterization of disease extent in prostate cancer patients," *Transl. Oncol.*, vol. 8, no. 1, pp. 25–34, Feb. 2015.

[16] A. J. Walker, J. Ruzevick, A. A. Malayeri, D. Rigamonti, M. Lim, K. J. Redmond, and L. Kleinberg, "Postradiation imaging changes in the CNS: How can we differentiate between treatment effect and disease progression?," *Future Oncology*. 2014.

[17] D. L. G. Hill, P. G. Batchelor, M. Holden, and D. J. Hawkes, "Medical image registration," *Physics in Medicine and Biology*, vol. 46, no. 3. pp. 173–178, 2001.

[18] R. Adams and L. Bischof, "Seeded Region Growing," *IEEE Trans. Pattern Anal. Mach. Intell.*, vol. 16, no. 6, pp. 641–647, 1994.

[19] P. Marquez-Neila, L. Baumela, and L. Alvarez, "A morphological approach to curvature-based evolution of curves and surfaces," *IEEE Trans. Pattern Anal. Mach. Intell.*, 2014.

[20] L. Álvarez, L. Baumela, P. Henríquez, and P. Márquez-Neila, "Morphological snakes," in *Proceedings of the IEEE Computer Society Conference on Computer Vision and Pattern Recognition*, 2010.

[21] V. Caselles, R. Kimmel, and G. Sapiro, "Geodesic Active Contours," *Int. J. Comput. Vis.*, 1997.

[22] T. F. Chan and L. A. Vese, "Active contours without edges," *IEEE Trans. Image Process.*, 2001.

[23] S. Osher and R. Tsai, "Level Set Methods and Their Applications in Image Science," *Commun. Math. Sci.*, 2003.

[24] F. Catté, F. Dibos, and G. Koepfler, "A morphological scheme for mean curvature motion and applications to anisotropic diffusion and motion of level sets," in *Proceedings - International Conference on Image Processing, ICIP*, 1994.